Published in final edited form as:
Inverse Probl. 2010 July 1; 26(7): 074009–. doi:10.1088/0266-5611/26/7/074009.

Contrast-enhanced microwave imaging of breast tumors: a computational study using 3-D realistic numerical phantoms

J D Shea, **P Kosmas**, **B D Van Veen**, and **S C Hagness**
Department of Electrical and Computer Engineering University of Wisconsin-Madison 1415 Engineering Drive Madison, WI 53706

J D Shea: jacob_shea@ieee.org

Abstract

The detection of early-stage tumors in the breast by microwave imaging is challenged by both the moderate endogenous dielectric contrast between healthy and malignant glandular tissues and the spatial resolution available from illumination at microwave frequencies. The high endogenous dielectric contrast between adipose and fibroglandular tissue structures increases the difficulty of tumor detection due to the high dynamic range of the contrast function to be imaged and the low level of signal scattered from a tumor relative to the clutter scattered by normal tissue structures. Microwave inverse scattering techniques, used to estimate the complete spatial profile of the dielectric properties within the breast, have the potential to reconstruct both normal and cancerous tissue structures. However, the ill-posedness of the associated inverse problem often limits the frequency of microwave illumination to the UHF band within which early-stage cancers have sub-wavelength dimensions. In this computational study, we examine the reconstruction of small, compact tumors in three-dimensional numerical breast phantoms by a multiple-frequency inverse scattering solution. Computer models are also employed to investigate the use of exogenous contrast agents for enhancing tumor detection. Simulated array measurements are acquired before and after the introduction of the assumed contrast effects for two specific agents currently under consideration for breast imaging: microbubbles and carbon nanotubes. Differential images of the applied contrast demonstrate the potential of the approach for detecting the preferential uptake of contrast agents by malignant tissues.

1. Introduction

Consideration of the safety, cost, availability, sensitivity, and specificity of established breast cancer screening methods such as mammography and magnetic resonance imaging (MRI) motivates interest in alternative or complementary technologies. The last decade has seen expansive investigation of a number of techniques in which the interior of the breast is probed noninvasively with low-power, microwave-frequency electromagnetic waves. The ultimate goal of this research is a safe, inexpensive, and accurate approach to the detection, monitoring, and assessment of breast cancers. Tissue-penetrating radar techniques have been applied to the tumor detection problem to locate strong scattering targets within the breast [1,2]. Electromagnetic inverse scattering has been widely investigated in application to breast imaging as such methods offer a complete mapping of the dielectric profile of the breast [3–11]. Inverse scattering approaches have been applied to data from numerical and experimental models of the breast, and some preliminary clinical studies have been performed [12,13].

The three-dimensional (3-D) imaging results presented in [9,11] were obtained with a frequency-domain inverse scattering algorithm formulated using the distorted Born iterative method (DBIM) [14]. The algorithm reconstructs the complete 3-D profile of the dielectric properties of the interior of the breast using multistatic array data measured over a discrete set

of frequencies. The imaging method was evaluated in [11] in application to realistic numerical breast phantoms of healthy tissues over a range of fibroglandular density classifications. The method was shown to produce representative reconstructions of the actual profile of complex permittivity, suggesting that it may be suitable for normal tissue density assessment. However, the low resolution of the images suggests that early-stage malignancies may not be identifiable by direct inspection of the images.

Endogenous contrast and spatial resolution are two important considerations in the detection and location of tumors by microwave imaging techniques. Recent studies of the histopathology and microwave-frequency dielectric properties of excised breast tissues suggested a much lower contrast between healthy and cancerous tissues than was previously understood [15]. The *ex-vivo* microwave dielectric properties of malignant glandular tissues were observed to be about ten times those of adipose tissue, but only one tenth higher than the properties of normal glandular tissues. Furthermore, the electrical dimension of early-stage cancers are at or below the nominal half-wavelength resolution limit of the UHF-band frequencies (0.3–3.0 GHz) typically employed in frequency-domain microwave inverse scattering. Although super-resolution has been observed and attributed to evanescent waves in near-field measurements or in multiple-scattering environments [16,17], microwave detection of early-stage malignancies is nevertheless challenged by the moderate endogenous dielectric contrast, the small scattering area of these malignancies, and the heterogeneous scattering environment of healthy glandular tissue in which tumors often form.

These fundamental challenges can be addressed in part through the use of comparative information, such as a contralateral comparison of a patient's left and right breasts [12], or the monitoring of tissue properties and distribution over time. A simple proof-of-concept of the latter approach was illustrated for a numerical breast phantom with and without a malignant inclusion [9]. Several medical imaging modalities have made use of contrast agents to enhance imaging in the areas of concentration of the agent. For example, breast malignancies are imaged in MRI with the introduction of a gadolinium contrast agent [18]. The preferential uptake of a contrast agent by malignant tissue [19,20] could enhance the contrast of the malignant tissue relative to the healthy surrounding tissue and allow microwave detection via comparative imaging using pre-and post-contrast measurements.

In this computational study we investigate the use of exogenous contrast agents in microwave imaging to detect tumors based on the change in their dielectric properties after the introduction of the agents. We assume an effective change in dielectric contrast as suggested by preliminary studies of two potential contrast agents for use in microwave breast imaging: microbubbles [21] and carbon nanotubes [22,23]. A homogeneous spherical inclusion is placed among healthy fibroglandular tissues in anatomically realistic numerical breast phantoms of varying fibroglandular density. The inclusion is given dielectric properties representative of either malignant tissue or malignant tissue under an assumed influence of a contrast agent. A Gauss-Newton nonlinear inverse scattering method is used to reconstruct 3-D estimates of the numerical phantom profiles in each case. Differential imaging then compares the estimated profiles to assess the tumor information available to this approach.

The challenges inherent to detecting small, compact breast tumors with microwaves are discussed in section 2 to motivate study of contrast agents. In section 3 we review the numerical breast phantoms which serve as the computational test beds for the imaging investigation and we summarize the reported effects of the contrast agents at microwave frequencies. Section 4 details the inverse scattering algorithm used to reconstruct the dielectric profiles of the numerical phantoms. We present imaging results in section 5 for three groups of numerical phantoms, each having a single tumor: homogeneous interiors, realistic heterogeneous

interiors, and realistic heterogeneous interiors with the tumor under the influence of a contrast agent. Further discussion and concluding remarks are offered in section 6.

2. Microwave Imaging of Small Tumors

Before turning our attention to the imaging of malignant inclusions in numerical breast phantoms, we first evaluate a fundamental dynamic affecting tumor detection performance in microwave imaging systems: the amount of scattering information available from the tumor depends primarily on the size of the tumor and the contrast of the tumor relative to the surrounding tissue. To illustrate these considerations, we compute the scattering cross-section of a lossy dielectric sphere as the diameter and contrast are varied. The scattering cross-section, as defined in [24], is the area of the incident plane-wave power density equal to the total power scattered from the sphere over all 4π steradians. The performance of inverse scattering techniques generally improves with additional information obtained by adding angles of illumination and multi-static observations to the system. Thus, the scattering cross section of an object is a measure of the relative amount of information available to an imaging system over a range of frequencies. In particular, it can illustrate the limitation of information from sub-resolution features and low contrast objects. The scattering cross-section given by equation (11–104) of [24] is evaluated and plotted in figure 1 versus electrical diameter for a sphere of malignant tissue in three different lossless background materials exhibiting relative permittivity values that span the range of normal breast tissue. The three background media are referred to as fibroglandular, transitional, and adipose; these representative normal breast tissue types are explained in further detail in section 3. In each case, figure 1 shows the sharp decline in scattering information in the region below the $\lambda/2$ resolution limit, where the scattering response from the tumor will be overtaken by errors, noise, and scattering from larger tissue structures. These curves also show that the low contrast of a tumor buried in normal fibroglandular tissue presents a scattering cross-section that decays below the physical cross-section above the nominal $\lambda/2$ resolution limit.

Inverse scattering is a model-based approach to microwave imaging that operates by comparing the computed scattering from an estimated object profile to the measured scattering from the actual object. In the case of an electrically small object, for which a resolution-limited reconstruction will overestimate the dimension of the object, figure 1 suggests that reconstructed contrast will be underestimated to limit the magnitude of the computed scattering response equal to that of the actual object. According to this reasoning, we expect a resolution-limited microwave breast imaging system to underestimate the properties of electrically small features of the tissue distribution, such as early-stage tumors. We illustrate this effect in section 5 by imaging a simple numerical breast phantom with a single spherical tumor of varying diameter placed in the three cases of homogeneous background tissue (normal fibroglandular, transitional, and adipose) considered in figure 1.

3. Testbeds and Data Generation

Measurements for our study are simulated using anatomically realistic numerical models from the University of Wisconsin Computational Electromagnetics Laboratory's (UWCEM) breast phantom repository [25,26]. In this section we summarize the models selected from the repository and the modifications made to these numerical phantoms to create the test beds employed in this paper. We present the endogenous frequency-dependent dielectric properties of the breast tissue models as well as the assumed effect of the microbubble and carbon nanotube contrast agents on the dielectric properties of malignant tissue.

3.1. Heterogeneous Numerical Breast Phantoms

We select one phantom from each of the four American College of Radiology classifications of fibroglandular breast tissue density [27]: ID number 071904 from the Class 1 group ("mostly fatty"), 010204 from the Class 2 group ("scattered heterogeneity"), 062204 from the Class 3 group ("heterogeneously dense"), and 012304 from the Class 4 group ("extremely dense"). The phantoms are defined on a 0.5-mm uniform Cartesian grid. The 1.5-mm-thick, homogeneous skin region of the repository phantoms is replaced by a 2.0-mm-thick region to match the cell dimension of our imaging grids. The dielectric properties of the constituent tissues of the MRI-derived phantoms are mapped as described by Zastow *et al.* [26]. We use a least-squares fit of the single-pole Debye relaxation model to the reported properties of *ex-vivo* breast tissues [28] over our frequency range of interest, 0.5 to 3.5 GHz. The single-pole Debye model for complex permittivity is given by,

$$\varepsilon_{\mathrm{rel}}(\omega)+\frac{\sigma_{\mathrm{eff}}(\omega)}{j\omega\varepsilon_{\mathrm{o}}}=\varepsilon_{\infty}+\frac{\Delta\varepsilon}{1+j\omega\tau}+\frac{\sigma_{\mathrm{s}}}{j\omega\varepsilon_{\mathrm{o}}} \tag{1}$$

The relaxation time constant, τ, of the Debye model is fixed at 15 ps for all tissues. The values of the Debye model parameters (infinite permittivity, ε_{∞}; delta permittivity, $\Delta\varepsilon$; static permittivity, $\varepsilon_{\mathrm{s}} = \varepsilon_{\infty} + \Delta\varepsilon$; and static conductivity, σ_{s}) for the breast tissue models in the phantoms are given in table 1. The table gives the range of parameters assigned to adipose, transitional, and fibroglandular tissue regions in the phantoms. The relative permittivity, $\varepsilon_{\mathrm{rel}}$, and effective conductivity, σ_{eff}, of these models are plotted over frequency in figure 2(a)–(b). The Debye parameters assigned to the homogeneous skin region [29] are also given in table 1. The phantom and array are immersed in a lossless medium with a relative permittivity similar to vegetable oil, $\varepsilon_{\mathrm{rel}} = 2.6$.

In this study we investigate the image reconstruction of a compact malignant mass. Since each phantom in the repository is comprised only of normal tissues, we add a homogeneous spherical inclusion having the median properties of malignant glandular breast tissue, as characterized by Lazebnik *et al.* [15] and given in table 1. A single 1-cm-diameter inclusion is placed adjacent to or within an area of fibroglandular tissue in each of the four test phantoms. A survey of the size of the tumors detected in a large collection of breast cancer studies of various modalities shows that the median diameter of detected tumors ranges between 10 to 20 mm [30]. Thus, a 1-cm diameter for the inclusion represents a clinically relevant dimension at which to evaluate tumor imaging performance. In addition, 1 cm is on the order of one half wavelength – the nominal resolution limit – in fibroglandular tissue at the upper frequencies of the UHF band.

To emulate an idealized preferential uptake of a contrast agent by malignant tissue, we vary the properties of the inclusion according to the contrast effects suggested by preliminary studies of two contrast agents. A computational study of air-filled microbubbles in malignant tissue [31] showed that the effective permittivity and conductivity were decreased by approximately 30% due to the presence of microbubbles at a concentration of 20% by volume – a concentration that is within the dosage of existing ultrasound procedures. We reduce the Debye parameters of the malignant inclusion accordingly to simulate this concentration of microbubbles; thus the frequency-averaged contrast of the Debye model given in table 1 for malignant tissue with microbubbles is −30% in both relative permittivity and effective conductivity relative to the endogenous properties. In the case of carbon nanotube contrast agents, we fit Debye models to the reported dielectric properties measurements for an experimental material mimicking the dielectric properties of malignant tissue with and without a 2 mg/mL concentration of carbon nanotubes [23]. The resulting frequency-averaged contrast of the Debye model given in table 1 for malignant tissue with carbon nanotubes is +22% in relative permittivity and +66% in

effective conductivity relative to the endogenous properties. The effect of each contrast agent on the dielectric properties of the malignant tissue model is plotted over frequency in figure 2 (c)–(d).

3.2. Homogeneous Numerical Breast Phantoms

An additional set of numerical phantoms is created by downsampling the Class 2 phantom from the 0.5-mm grid to a 2.0-mm grid. The interior of the downsampled phantom is replaced by a homogeneous material described by one of three Debye models representative of nominal properties of each tissue type: normal fibroglandular tissue (ε_∞=17.5, $\Delta\varepsilon$=31.6, σ_s=0.720), transitional tissue (ε_∞=10.5, $\Delta\varepsilon$=11.7, σ_s=0.273), or adipose (ε_∞=3.11, $\Delta\varepsilon$=1.70, σ_s=0.0367). A single homogeneous spherical inclusion having the endogenous properties of malignant tissue given in table 1 is placed in the homogeneous interior.

3.3. Data Acquisition

A 40-element cylindrical array of 14-mm dipoles surrounds each numerical test phantom, as shown in figure 3. The antennas are distributed on five elliptical rings of eight antennas each, with adjacent rings rotated by $\pi/8$. The rings are evenly spaced between the posterior and anterior coronal planes of each phantom. The dimensions of each array are set to provide a minimum spacing of 1 cm between each antenna element and the skin surface.

Array measurements of the phantoms are simulated using the finite-difference time-domain (FDTD) numerical method. An auxiliary differential equation approach [32] is used to simulate Debye relaxation in the dispersive dielectric materials, and a perfectly matched layer [32] is used to terminate the grid. The dipole antennas are driven with a modulated Gaussian pulse having a bandwidth covering 0.5 to 3.5 GHz. Each antenna is sourced individually in independent simulations and the time-domain received fields are recorded at every antenna and converted to phasors at the frequencies of interest via the discrete Fourier transform.

Data is acquired from each of the four numerical phantoms from the repository for three cases of the dielectric properties of the spherical inclusion: the endogenous malignant properties, decreased properties due to microbubbles, and increased properties due to carbon nanotubes. Data is also acquired from the downsampled Class 2 phantom for each of three cases of homogeneous interior background properties. The diameter of the inclusion in the breast interior is varied from 2 mm to 22 mm in 4 mm increments. Simulations of the downsampled phantom are conducted on the same 2-mm grid used by the reconstruction algorithm in order to remove modeling error from the evaluation. These simulated measurement sets are used to evaluate resolution and estimation error of the imaging system.

White Gaussian noise is added to the simulated data such that the signal-to-noise ratio (SNR) is 50 dB. The reference signal level is defined at each frequency as the mean of the measured total fields over all multi-static measurements of the numerical phantom – typically about 60 dB below the source level for the inefficient and unmatched antenna models used in this study. This level of noise is comparable to the noise levels specified in prior experimental and numerical microwave breast imaging studies [8,10,33].

4. Imaging Methodology

In section 4.1, we briefly review the well-known theoretical relationship between the field scattered from a domain of unknown objects and the dielectric profile of that domain, and formulate an approximate discrete linear system of equations using multi-static array observations at multiple frequencies. The linear system is constrained by restricting the frequency dependence of the solution to the space of single-pole Debye solutions. An iterative

method for solving the nonlinear scattering problem is summarized in section 4.2, and a simple approach to creating a differential image from two sets of measurements is presented in section 4.3.

4.1. Electromagnetic Inverse Scattering

The scattering of electromagnetic radiation from a non-magnetic, heterogeneous dielectric object domain $\mathcal{V}$ at an observation location described by coordinate vector $\mathbf{r}_{\text{obs}}$ can be written as an volume integral equation,

$$\mathbf{E}^s(\mathbf{r}_{\text{obs}}) = k_0^2 \int_{\mathcal{V}} \overline{\mathbf{G}}^b(\mathbf{r}_{\text{obs}}|\mathbf{r}')\mathbf{E}^t(\mathbf{r}')\,[\varepsilon(\mathbf{r}') - \varepsilon^b(\mathbf{r}')]\,d\mathbf{r}' \tag{2}$$

where the scattered field, $\mathbf{E}^s$, is the difference between the total field observed in the object environment and the total field observed in the background environment. The scattered field results from the re-radiation of the total field, $\mathbf{E}^t$, in $\mathcal{V}$ from the dielectric contrast formed by the difference between the object profile, $\varepsilon(\mathbf{r})$, and the background dielectric profile, $\varepsilon^b(\mathbf{r})$. The free-space wavenumber is k_0. The scattering contribution at $\mathbf{r}_{\text{obs}}$ due to the dielectric contrast at $\mathbf{r} \in \mathcal{V}$ is determined by the Green's function, $\overline{\mathbf{G}}^b(\mathbf{r}_{\text{obs}}|\mathbf{r})$, of the background dielectric profile. The object and background profiles are complex permittivities and both may be heterogeneous.

The total field, $\mathbf{E}^t$, in $\mathcal{V}$ depends on the multiple scattering interactions between the features of the dielectric profile. The scattered field, $\mathbf{E}^s$, is therefore nonlinearly related to the contrast function due to the product $\mathbf{E}^t(\mathbf{r})\,[\varepsilon(\mathbf{r}) - \varepsilon^b(\mathbf{r})]$ in the integrand of (2). The relation can be linearized using the Born approximation [14], in which $\mathbf{E}^t$ in $\mathcal{V}$ is approximated by the background field $\mathbf{E}^b$, that is, the total field in the background profile $\varepsilon^b(\mathbf{r})$.

The volume $\mathcal{V}$ enclosing the unknown object volume can be discretized by the set of constant basis functions of edge length Δ given by

$$\varphi_k(\mathbf{r}) = \begin{cases} 1 & \text{for } \| \mathbf{r}_k - \mathbf{r} \|_\infty \le \frac{\Delta}{2} \\ 0 & \text{for otherwise} \end{cases} \tag{3}$$

for all $\mathbf{r}_k = \Delta\,[(l_k + \tfrac{1}{2})\,\mathbf{a}_x + (m_k + \tfrac{1}{2})\,\mathbf{a}_y + (n_k + \tfrac{1}{2})\,\mathbf{a}_z] \in \mathcal{V}, (l, m, n) \in N^3$. Using this basis for voxels $k = 1, \ldots, K$ within $\mathcal{V}$, the unknown contrast function can be written as a length K vector of basis coefficients, $\mathbf{v}$, where $v_k = \frac{1}{\Delta^3} \int_{\mathcal{V}} \left[\varepsilon(\mathbf{r}) - \varepsilon^b(\mathbf{r})\right] \varphi_k(\mathbf{r})\,d\mathbf{r}'$. The Born approximation of (2) can then be written as a discrete vector equation. Noting the vector form of the scattered field, $\mathbf{E}^s(\mathbf{r}_{\text{obs}}) = \begin{bmatrix} E_x^s & E_y^s & E_z^s \end{bmatrix}^T$, the linearized vector scattering equation for a source at $\mathbf{r}_{\text{src}}$ is $\mathbf{E}^s = \mathbf{H}\mathbf{v}$, where $\mathbf{H}$ is the $3 \times K$ matrix given by,

$$\mathbf{H} = k_0^2 \Delta^3 [\overline{\mathbf{G}}^b(\mathbf{r}_{\text{obs}}|\mathbf{r}_1)\mathbf{E}^b(\mathbf{r}_1|\mathbf{r}_{\text{src}}) \cdots \overline{\mathbf{G}}^b(\mathbf{r}_{\text{obs}}|\mathbf{r}_K)\mathbf{E}^b(\mathbf{r}_K|\mathbf{r}_{\text{src}})]. \tag{4}$$

A set of field observations due to a source at $\mathbf{r}_{\text{src}}$, as well as additional sets of field observations due to other source locations, can be used to create a larger system of equations in the unknown $\mathbf{v}$, where the vector scattering equations for each of M multi-static observations are combined into a length $3M$ vector, $\mathbf{e}^s$, and a $3M \times K$ matrix, $\mathbf{B}$. In practice, fields are typically measured by single-polarization antennas. We therefore consider only the scalar field observations, E^s,

made by an array of *z*-directed dipoles. In this case $\mathbf{e}^s$ is only length *M*. In either the scalar or vector observation case, the matrices associated with each observation are collected as the block-rows of a larger matrix, $\mathbf{B}=\begin{bmatrix} \mathbf{H}_1^T & \mathbf{H}_2^T & \cdots & \mathbf{H}_M^T \end{bmatrix}^T$, operating on the same unknown contrast function vector, **v**, such that $\mathbf{e}^s = \mathbf{B}\mathbf{v}$.

Observations at multiple frequencies can be added to the linear system of scattering equations by vertically concatenating the multiple-observation vectors, $\mathbf{e}^s(\omega)$, and matrices, $\mathbf{B}(\omega)$, at each of *F* frequencies. The resulting $MF \times K$ system is less ill-posed than a single-frequency system [34] and can be approximately inverted to yield a simultaneous solution for a frequency-independent contrast function **v**. When the actual dielectric profile is frequency-dependent, the system can be transformed by a parametric model of the frequency dependence [6]. For a general parametric model of complex permittivity, $\varepsilon(\omega)=\mathcal{F}(\omega, p_1, p_2, \ldots)$, the multiple-observation linear scattering system at each frequency is transformed to,

$$\mathbf{e}^s(\omega)=\begin{bmatrix} \frac{d\mathcal{F}}{dp_1}\mathbf{B}(\omega) & \frac{d\mathcal{F}}{dp_2}\mathbf{B}(\omega) & \cdots \end{bmatrix} \begin{bmatrix} \mathbf{p}_1 - \mathbf{p}_1^b \\ \mathbf{p}_2 - \mathbf{p}_2^b \\ \vdots \end{bmatrix} \tag{5}$$

We choose the Debye relaxation model of (1) for the parametric model of the contrast function to fit the dispersive properties of biological tissues. Note that the coefficients $d\mathcal{F}/dp$ must be constant so that the system remains linear in the unknown parameters. Since $d\mathcal{F}/dt$ is a function of τ in the Debye model, we therefore assume a fixed value for the time constant. The remaining three degrees of freedom in the model are sufficient to accurately capture the frequency dependence of the tissues over the frequency range of interest. Further, noting that the Debye parameters are real-valued we split each complex equation into real and imaginary parts so that the solution space is limited to real values. Using (5) and the three-parameter Debye model (1) for the contrast function, $\varepsilon(\omega) - \varepsilon^b(\omega)=\mathcal{F}(\omega, \varepsilon_\infty, \Delta\varepsilon, \sigma_s) - \mathcal{F}(\omega, \varepsilon_\infty^b, \Delta\varepsilon^b, \sigma_s^b)$, a $2MF \times 3K$ system is obtained.

$$\begin{bmatrix} \Re\{\mathbf{e}^s(\omega_1)\} \\ \vdots \\ \Re\{\mathbf{e}^s(\omega_F)\} \\ \Im\{\mathbf{e}^s(\omega_1)\} \\ \vdots \\ \Im\{\mathbf{e}^s(\omega_F)\} \end{bmatrix} = \begin{bmatrix} \Re\left\{\begin{bmatrix} \frac{d\mathcal{F}}{d\varepsilon_\infty}\mathbf{B}(\omega_1) & \frac{d\mathcal{F}}{d\Delta\varepsilon}\mathbf{B}(\omega_1) & \frac{d\mathcal{F}}{d\sigma_s}\mathbf{B}(\omega_1) \end{bmatrix}\right\} \\ \vdots \\ \Re\left\{\begin{bmatrix} \frac{d\mathcal{F}}{d\varepsilon_\infty}\mathbf{B}(\omega_F) & \frac{d\mathcal{F}}{d\Delta\varepsilon}\mathbf{B}(\omega_F) & \frac{d\mathcal{F}}{d\sigma_s}\mathbf{B}(\omega_F) \end{bmatrix}\right\} \\ \Im\left\{\begin{bmatrix} \frac{d\mathcal{F}}{d\varepsilon_\infty}\mathbf{B}(\omega_1) & \frac{d\mathcal{F}}{d\Delta\varepsilon}\mathbf{B}(\omega_1) & \frac{d\mathcal{F}}{d\sigma_s}\mathbf{B}(\omega_1) \end{bmatrix}\right\} \\ \vdots \\ \Im\left\{\begin{bmatrix} \frac{d\mathcal{F}}{d\varepsilon_\infty}\mathbf{B}(\omega_F) & \frac{d\mathcal{F}}{d\Delta\varepsilon}\mathbf{B}(\omega_F) & \frac{d\mathcal{F}}{d\sigma_s}\mathbf{B}(\omega_F) \end{bmatrix}\right\} \end{bmatrix} \begin{bmatrix} \varepsilon_{\infty 1} - \varepsilon_{\infty 1}^b \\ \vdots \\ \varepsilon_{\infty K} - \varepsilon_{\infty K}^b \\ \Delta\varepsilon_1 - \Delta\varepsilon^b{}_1 \\ \vdots \\ \Delta\varepsilon_K - \Delta\varepsilon^b{}_K \\ \sigma_{s1} - \sigma_{s1}^b \\ \vdots \\ \sigma_{sK} - \sigma_{sK}^b \end{bmatrix} \tag{6}$$

We will denote the system in (6) as $\mathbf{y} = \mathbf{A}\mathbf{x}$. It is a multi-static, multiple-frequency, linearized description of the scattering due to the contrast function, formulated in the Debye parameter space. The solution of this system, described below, yields an estimate of the contrast function of the unknown object.

4.2. Distorted Born Iterative Method

The linear system $\mathbf{y} = \mathbf{A}\mathbf{x}$ of (6) approximates the nonlinear scattering relation of (2). The error in the Born approximation used to linearize (2) increases with the magnitude of the contrast function. The high contrasts between the constituent breast tissues of table 1 will result in a highly inaccurate solution based on the Born approximation alone. However, a nonlinear method of optimization can be used to overcome the limitation. The distorted Born iterative method (DBIM) [14], a form of Gauss-Newton optimization [35], is the approach we use here to estimate the contrast function from the observations of nonlinear scattering. This method iteratively refines the estimate, beginning with an initial guess for the background profile that may include any available *a priori* information about the object profile. A solution to (6) (the *inverse solution*) is found at each iteration i to obtain an update to the estimated profile. The updated estimate, $\hat{\varepsilon}_i(\mathbf{r})$, is used as the background profile, $\varepsilon^b(\mathbf{r})$, in the subsequent iteration and the background fields and Green's functions are recomputed (the *forward solution*). The difference in the scattering from the background profile and the object profile decreases at each iteration as the estimate is improved. The DBIM algorithm is terminated when the norm of the residual scattering, $\|\mathbf{y}\|$, converges sufficiently. The full DBIM procedure is outlined in Algorithm 1.

We use the FDTD method in the forward solution to efficiently compute the background fields and Green's functions at multiple frequencies. The FDTD simulations are performed as described in section 3 for the acquisition of measurements with the exception that the grid dimension in the forward model is 2.0 mm. The cells of the forward solution grid are the same as the voxels defined in (3), extended $\forall\, k : \mathbf{r}_k \in \mathcal{D}$, where $\mathcal{D}$ is a cuboid measurement region enclosing $\mathcal{V}$ and the array of N antennas. The forward solution domain is depicted by the 3-D diagram in figure 3. In addition, the background field due to each source, $\mathbf{E}^b(\mathbf{r}_k|\mathbf{r}_{\text{src}})$, is measured at each cell $\mathbf{r}_k \in \mathcal{V}$. The heterogeneous background Green's function is computed using the principle of reciprocity [36] and the field measured at $\mathbf{r}_k \in \mathcal{V}$ due to a source current I_x, I_y, or I_z of length Δ at $\mathbf{r}_{\text{src}} \in \mathcal{D}$.

$$\overline{\mathbf{G}}^b(\mathbf{r}_{\text{obs}}|\mathbf{r}_k) = \frac{j}{\omega\mu\Delta}\begin{bmatrix} \frac{1}{I_x}E_x^b(\mathbf{r}_k)\big|_{I_y,I_z=0} & \frac{1}{I_x}E_x^b(\mathbf{r}_k)\big|_{I_y,I_z=0} & \frac{1}{I_x}E_x^b(\mathbf{r}_k)\big|_{I_y,I_z=0} \\ \frac{1}{I_y}E_x^b(\mathbf{r}_k)\big|_{I_x,I_z=0} & \frac{1}{I_y}E_y^b(\mathbf{r}_k)\big|_{I_x,I_z=0} & \frac{1}{I_y}E_z^b(\mathbf{r}_k)\big|_{I_x,I_z=0} \\ \frac{1}{I_z}E_x^b(\mathbf{r}_k)\big|_{I_x,I_y=0} & \frac{1}{I_z}E_y^b(\mathbf{r}_k)\big|_{I_x,I_y=0} & \frac{1}{I_z}E_z^b(\mathbf{r}_k)\big|_{I_x,I_y=0} \end{bmatrix} \tag{7}$$

The antenna array described in section 3 consists of z-oriented dipoles sourced with I_z. Thus, only the last row of the Green's function tensor of (7) is computed.

The inverse solution is the inexact Newton step found using the conjugate gradient for least-squares (CGLS) inversion method [37], which finds a solution to the system of normal equations, $\mathbf{A}^T\mathbf{y} = \mathbf{A}^T\mathbf{A}\mathbf{x}$. The inverse solution approximates the contrast updates for each voxel $\mathbf{r}_k \in \mathcal{V}$. The update step length is fixed at unity. The under-determined system in (6) is ill-posed and requires regularization. Regularization is accomplished by early termination of the CGLS algorithm after a fixed number of iterations [8,11]. The termination condition is based on empirical observations of the trade-off between reduction of the norm of the residual scattering, $\|\mathbf{y}\|$, and the divergent growth of the norm of the unknown contrast function, $\|\mathbf{x}\|$, that is indicative of the corruption of the solution by noise and other errors.

4.3. Differential Imaging

A small change in contrast or a change to a localized area of the object profile may not be recognizable among the more sizable features of the reconstruction. The effect of a change in

the object profile on the reconstructed profile can be visualized by the difference between the reconstructed profiles before and after the change. In this way, not only is the location of the change revealed but the ability of the system to measure information from that change is confirmed. Thus, by imaging the difference between the reconstructions of the phantoms before and after the introduction of a contrast agent, we evaluate both the scattering information available from a change in contrast of a compact malignant inclusion as well as the ability of the method to locate that change.

First, we simulate measurements of a phantom containing a malignant lesion with endogenous dielectric properties. Next, we assume a change in dielectric properties of the inclusion due to the contrast agents as detailed in table 1 and simulate a second set of measurements. The "before" and "after" measurements are then individually reconstructed by the DBIM, and the difference between the two reconstructions is imaged.

5. Results

We begin with the reconstruction of the downsampled homogeneous numerical phantom modified described in section 3.2. We then present images of the reconstruction of the four realistic heterogeneous numerical phantoms, each having a single inclusion of malignant tissue with endogenous properties. Finally, we present the differential images of all four realistic phantoms, using the reconstructions of each with and without the effect of the contrast agent applied to the properties of the inclusion.

In all cases presented in this paper, the linear system is constructed with data acquired at 1.0, 1.5, 2.0, and 2.5 GHz from all multistatic array channels, excluding the monostatic channels. For each phantom, the initial background profile of the breast interior is a homogeneous interior having the average properties of the true phantom profile and includes a downsampled version of the skin region of the true phantom. The unknown imaging region ν is defined to be the interior breast volume inside the skin layer. The dielectric properties of the immersion and skin regions are assumed known *a priori*. The DBIM is terminated after the 8^{th} step and the CGLS algorithm is terminated at the 5^{th} iteration at every step of the DBIM. These conditions ensure convergence at termination in all the cases shown such that the decrease in the residual scattering norm, $||y||$, is less than 1% of the residual scattering norm of the initial step. The CGLS termination condition is based on the results of an L-curve heuristic used for imaging these numerical phantoms in [11]. All imaging results are visualized in orthogonal cross-sections of the profiles of relative permittivity and effective conductivity at 2.5 GHz, computed according to (1) from the reconstructed profiles of the Debye parameters.

On the 2-mm voxel grid, the forward domains of the four realistic numerical phantoms contain between roughly 500,000 and 1,000,000 cells while the inverse domain contains between roughly 120,000 and 360,000 unknowns. The forward solution is executed on a 128-core GPU using Acceleware's FDTD API, while the inverse solution is executed on a 4-core CPU using MATLAB code. The 40 independent simulations of the forward solution are run in serial on the GPU, each taking 20 to 30 seconds. The inverse solution requires about 3 minutes on a memory-limited system, for a total time per step of the DBIM of around 20 minutes. Parallelization of the forward simulations, implementation of the inverse solution on the GPU, and advances in GPU performance are expected to reduce the time per DBIM iteration by about a factor of ten [38].

5.1. Imaging a Tumor in a Homogeneous Phantom Interior

The simplified breast model consisting of a skin region, a homogeneous background in the interior breast volume, and a single spherical inclusion is imaged over all combinations of three background tissue types (adipose, transitional, and fibroglandular tissue properties) and six

diameters (2, 6, 10, 14, 18, and 22 mm) of a homogeneous inclusion with malignant tissue properties. The effect of inclusion diameter on the estimation accuracy is shown in figure 4 by comparison of the coronal cross-sections of the reconstructed relative permittivity at 2.5 GHz of inclusion diameters 6, 14, and 22 mm in a transitional tissue background. The error in the estimate is normalized by comparing the estimated Debye curves to the actual curve relative to the initial guess curve, $(\varepsilon^* - \hat{\varepsilon})/(\varepsilon^* - \varepsilon^0)$, averaged over the frequencies used in the reconstruction. The real and imaginary parts of the error are computed separately and are plotted in figure 5 versus the diameter of the inclusion. The peak of the estimated contrast for each case of inclusion diameter and background tissue is compared to the actual contrast in table 2.

These results show the improvement in the estimation accuracy of the imaging system as the inclusion diameter is increased through a range of sub-wavelength dimensions. The diameters are given in wavelengths in figure 5 and table 2 to demonstrate the dependence of estimation accuracy on the electrical dimension of the scatterer in a given background tissue. For example, despite the higher contrast of the inclusion in an adipose background, the longer wavelength (compared to that of other background tissues) results in increased estimation error. Thus, the sensitivity of tumor detection in the microwave imaging system will depend not only on the tumor contrast but also the wavelength in the tissue surrounding the tumor.

5.2. Imaging a Tumor in a Heterogeneous Phantom Interior

In the Class 1 and 2 phantoms the inclusion is placed adjacent to areas of both adipose and fibroglandular tissue, while in the Class 3 and 4 phantoms the inclusion is mostly surrounded by fibroglandular tissues. Table 2 and figure 5 suggest that a 10 mm inclusion will not be well reconstructed in a background of primarily adipose tissue, and that while the same inclusion in a background of dense fibroglandular tissue may be more accurately reconstructed, the low contrast and the low imaging resolution may blur it into adjacent features of the heterogeneous background. These predictions are confirmed in figures 6, 7, 8, and 9, where the reconstructions of the four realistic phantoms introduced in section 3 are compared to the actual phantom profiles. While the areas of dense fibroglandular heterogeneity are reconstructed, there is no clear visual evidence of the inclusion in any of the four reconstructions. These imaging results illustrate the expected challenges in directly imaging electrically small tumors, and motivate the use of contrast agents in microwave imaging.

5.3. Differential Imaging of a Tumor in a Heterogeneous Phantom Interior

Differential images showing the effect of each contrast agent on the reconstruction of relative permittivity and effective conductivity in each of the four realistic phantoms are shown in figures 10, 11, 12, and 13. These images are produced by subtracting the profiles reconstructed with and without the effect of the contrast agents. The cross-sections are taken through the voxel having the peak estimated contrast and the values are clipped at zero since the direction of the change in contrast caused by each agent is known. The white '×' marker on each cross-section marks the true location of the center of the inclusion, as projected onto the cross-sectional planes of the estimated location. The estimated change in contrast of the inclusion and the error in the estimated location of the inclusion are given in table 3 for each agent in each phantom.

In all cases, the differential images clearly show a compact change in the contrast of both relative permittivity and effective conductivity. The change is well resolved in all three dimensions, with some smearing along the coronal axis caused by the incomplete illumination of the breast by the cylindrical antenna array geometry. The error of the estimated location of the peak change in contrast is on the order of 10 mm or less and there is no discernible trend in the location error relative to the fibroglandular density of the phantom. The change in the

dielectric properties of the inclusion is underestimated in all cases, consistent with the prediction of both the scattering analysis of section 2 and the reconstructions of the homogeneous phantoms with 1.0 cm inclusions. The estimated change in properties are about 10–20% of the actual change in Class 2, 3, and 4 phantoms, while the estimate was only a few percent of the actual change in the mostly-fatty Class 1 phantom.

As noted in section 3, the data used in the reconstructions of the heterogeneous numerical phantoms include additive white Gaussian noise to create a 50 dB SNR. The effect of the noise on the difference images is evaluated over a range of noise levels. The perturbation of a difference image due to the noise is evaluated by subtracting the noiseless difference image from the noise-corrupted difference image. The peak noise perturbation for each numerical phantom is plotted in figure 14 for SNR from 10 to 50 dB. Comparison of these curves to the peak of the tumor spot in the difference images of figures 10a, 11a, 12a, and 13a, suggests accurate tumor identification in all cases studied for SNR greater than approximately 40 dB. We note that the image noise is higher in the reconstructions of the dense heterogeneous Class 3 and Class 4 tissue distributions since they reach higher dielectric properties over a more extensive fibroglandular distribution.

6. Discussion and Conclusion

The issue of the limited resolution of the imaging system has been carefully considered in this investigation. It is important to note, however, the role of the regularization technique in determining the detection sensitivity of the system. That the small tumors are not visible in the images of figures 6–9 is a consequence of both the loss of scattering information predicted by figure 1 as the tumor dimension decreases and the low-pass spatial filtering effect of the regularization technique employed in our algorithm. While there exist various edge-preserving approaches to regularization and global optimization techniques that can sharpen the resolution of the imaging system, there remains a fundamental issue of information deficiency that is independent of such techniques. Namely, as the dimension of a tumor decreases into the regime below one half-wavelength, the magnitude of the scattering decays exponentially until it decreases below the measurement sensitivity of the system. The problem of low level scattering information can exist even at larger dimensions due to the low dielectric contrast between malignant tissue and the surrounding healthy glandular tissue. In this work we have addressed the deficiency through the enhancement of tumor contrast by exogenous contrast agents, and the use of a differential imaging scheme to capture their effect.

There are practical issues to be considered in a real-world implementation of a differential imaging scheme. The assumptions of the contrast available from the agents and the selective uptake of the contrast agent in cancerous tissue are supported in the literature, but require further confirmation in a clinical setting. A differential image will reveal not only the change in the reconstruction due to a contrast agent but will also include artifacts due to any changes in the test fixture, location and position of the breast, noise, and any other measurement uncertainties. Our numerical models idealize many of these considerations, but provide an initial test bed in which to study the potential performance of a differential imaging scheme. Note that the assumed endogenous contrast between malignant and normal glandular tissue used in this initial test bed is based on *ex vivo* measurements and may differ slightly from the actual *in vivo* endogenous contrast.

Our analysis and results have illustrated the dynamics of tumor detection with respect to contrast and resolution in microwave imaging, particularly in the lower microwave frequencies often employed for inverse scattering solutions. The differential images demonstrate a successful approach by which contrast agents can be used in conjunction with microwave imaging to detect tumors, including compact tumors of dimensions below the nominal

resolution of the imaging system. The results of our investigation suggest a promising direction for further research on contrast-enhanced tumor detection by microwave imaging.

Microwave breast imaging has been an active research area over the past two decades and has received considerable recent attention. As supported by the results and discussion in this paper, there are a number of fundamental and contemporary issues deserving of further consideration in ongoing research of the microwave modality. Resolution remains an important issue and its fundamental dependence on wavelength, contrast, and measurement sensitivity points to potential avenues towards improving microwave detection performance by improving the information content of the measurement data. In addition, there remains significant opportunity for improvement of the performance through selection and development of imaging methods, including techniques of regularization, optimization, solution constraints, and modeling. Image validation is another important requirement in the development of microwave imaging. Computational studies are easily validated since the exact object is directly available for comparison; experimental studies offer practical measurement challenges with less realistic phantoms; clinical studies offer the best possible test case as well as perhaps the most challenging case for validation due to uncertainty of the true dielectric properties distribution. Lastly, there is a need for increased attention to the qualification of the potential clinical value of the microwave modality for medical imaging, including applications in screening, risk assessment, and tumor detection.

Acknowledgments

This work was supported by the National Institutes of Health under grant R01 CA112398 awarded by the National Cancer Institute.

References

1. Li X, Bond EJ, Van Veen BD, Hagness SC. An overview of ultrawideband microwave imaging via space-time beamforming for early-stage breast cancer detection. IEEE Antennas and Propagation Magazine February;2005 47(1):19–34.
2. Sill JM, Fear EC. Tissue sensing adaptive radar for breast cancer detection - experimental investigation of simple tumor models. IEEE Trans Microw Theory Tech November;2005 53(11):3312–3319.
3. Bulyshev AE, Semenov SY, Souvorov AE, Svenson RH, Nazarov AG, Sizov YE, Tatsis GP. Computational modeling of three-dimensional microwave tomography of breast cancer. IEEE Trans Biomed Eng September;2001 48(9):1053–1056. [PubMed: 11534841]
4. Li D, Meaney PM, Paulsen KD. Conformal microwave imaging for breast cancer detection. IEEE Trans Microw Theory Tech Apr;2003 51(4):1179–1186.
5. Fang Q, Meaney PM, Geimer SD, Streltsov AV, Paulsen KD. Microwave image reconstruction from 3-D field coupled to 2-D parameter estimation. IEEE Trans Med Imag April;2004 23(4):475–484.
6. Fang Q, Meaney PM, Paulsen KD. Microwave image reconstruction of tissue property dispersion characteristics utilizing multiple-frequency information. IEEE Trans Microw Theory Tech 2004;52 (8):1866–1875.
7. Zhang ZQ, Liu QH. Three-dimensional nonlinear image reconstruction for microwave biomedical imaging. IEEE Trans Biomed Eng 2004;51(3):544–548. [PubMed: 15000387]
8. Rubæk T, Meaney PM, Meincke P, Paulsen KD. Nonlinear microwave imaging for breast-cancer screening using Gauss-Newton's method and the CGLS inversion algorithm. IEEE Trans Antennas Propag August;2007 55(8):2320–2331.
9. Winters DW, Shea JD, Kosmas P, Van Veen BD, Hagness SC. Three-dimensional microwave breast imaging: Dispersive dielectric properties estimation using patient-specific basis functions. IEEE Trans Med Imag July;2009 28(7):969–981.
10. Gilmore C, Abubakar A, Hu Wenyi, Habashy TM, van den Berg PM. Microwave biomedical data inversion using the finite-difference contrast source inversion method. IEEE Trans Antennas Propag May;2009 57(5):1528–1538.

11. Shea JD, Kosmas P, Van Veen BD, Hagness SC. Three-dimensional microwave imaging of realistic numerical breast phantoms via a multiple-frequency inverse scattering technique. Medical Physics. 20102009 in press.
12. Poplack SP, Tosteson TD, Wells WA, Pogue BW, Meaney PM, Hartov A, Kogel CA, Soho SK, Gibson JJ, Paulsen KD. Electromagnetic breast imaging: Results of a pilot study in women with abnormal mammograms. Radiology May;2007 243(2):350–359. [PubMed: 17400760]
13. Meaney PM, Fanning MW, Raynolds T, Fox CJ, Fang QQ, Kogel CA, Poplack SP, Paulsen KD. Initial clinical experience with microwave breast imaging in women with normal mammography. Academic Radiology February;2007 14(2):207–218. [PubMed: 17236994]
14. Chew, WC. Waves and Fields in Inhomogeneous Media. IEEE Press; Piscataway, NJ: 1995.
15. Lazebnik M, Popovic D, McCartney L, Watkins CB, Lindstrom MJ, Harter J, Sewall S, Ogilvie T, Magliocco A, Breslin TM, Temple W, Mew D, Booske JH, Okoniewski M, Hagness SC. A large-scale study of the ultrawideband microwave dielectric properties of normal, benign, and malignant breast tissues obtained from cancer surgeries. Phys Med Biol 2007;52:6093–6115. [PubMed: 17921574]
16. Chen F, Chew WC. Experimental verification of super resolution in nonlinear inverse scattering. Applied Physics Letters 1998;72(23):3080–3082.
17. Cui TJ, Chew WC, Yin XX, Hong W. Study of resolution and super resolution in electromagnetic imaging for half-space problems. IEEE Trans Antennas Propag jun;2004 52(6):1398–1411.
18. Kuhl CK. MRI of breast tumors. Eur Radiol January;2000 10(1):46–58. [PubMed: 10663717]
19. Maeda, H. The enhanced permeability and retention (EPR) effect in tumor vasculature: The key role of tumor-selective macromolecular drug targeting. In: Weber, G., editor. Advances in Enzyme Regulation, Vol 41, volume 41 of Advances in Enzyme Regulation. 2001. p. 189-207.
20. Liu Z, Cai W, He L, Nakayama N, Chen K, Sun X, Chen X, Dai H. In vivo biodistribution and highly efficient tumour targeting of carbon nanotubes in mice. Nature Nanotechnology January;2007 2(1): 47–52.
21. Mashal A, Booske JH, Hagness SC. Towards contrast-enhanced microwave-induced thermoacoustic imaging of breast cancer: An experimental study of the effects of microbubbles on simple thermoacoustic targets. Phys Med Biol 2009;54:641–650. [PubMed: 19124946]
22. Mashal, A.; Sitharaman, B.; Booske, JH.; Hagness, SC. Dielectric characterization of carbon nanotube contrast agents for microwave breast cancer detection. Proceedings of the IEEE International Symposium on Antennas and Propagation; Charleston, SC. June 2009;
23. Mashal A, Sitharaman B, Li X, Avti P, Sahakian AV, Booske JH, Hagness SC. Toward carbon-nanotube-based theranostic agents for microwave detection and treatment of breast cancer: Enhanced dielectric and heating response of tissue-mimicking materials. IEEE Trans Biomed Eng. 2010 in press.
24. Ishimaru, A. Electromagnetic Wave Propagation, Radiation, and Scattering. Prentice Hall; Englewood Cliffs, NJ: 1991.
25. UWCEM Numerical Breast Phantom Repository. http://uwcem.ece.wisc.edu
26. Zastrow E, Davis SK, Lazebnik M, Kelcz F, Van Veen BD, Hagness SC. Development of anatomically realistic numerical breast phantoms with accurate dielectric properties for modeling microwave interactions with the human breast. IEEE Trans Biomed Eng December;2008 55(12):2792–2800. [PubMed: 19126460]
27. D'Orsi, CJ.; Bassett, LW.; Berg, WA. Breast Imaging Reporting and Data System: ACR BI-RADS-Mammography. 4. American College of Radiology; Reston, VA: 2003.
28. Lazebnik M, McCartney L, Popovic D, Watkins CB, Lindstrom MJ, Harter J, Sewall S, Magliocco A, Booske JH, Okoniewski M, Hagness SC. A large-scale study of the ultrawideband microwave dielectric properties of normal breast tissue obtained from reduction surgeries. Phys Med Biol 2007;52:2637–2656. [PubMed: 17473342]
29. Gabriel S, Lau RW, Gabriel C. The dielectric properties of biological tissues: III. Parametric models for the dielectric spectrum of tissues. Phys Med Biol 1996;41:2271–2293. [PubMed: 8938026]
30. Michaelson JS, Satija S, Kopans D, Moore R, Silverstein M, Comegno A, Hughes K, Taghian A, Smith B, Powell S. Gauging the impact of breast carcinoma screening in terms of tumor size and death rate. Cancer 2003;98(10):2114–2124. [PubMed: 14601080]

31. Lazebnik, M.; Booske, JH.; Hagness, SC. URSI General Assembly. Chicago, IL: Aug. 2008 Dielectric-properties contrast enhancement for microwave breast cancer detection: Numerical investigations of microbubble contrast agents.

32. Taflove, A.; Hagness, SC. Computational Electrodynamics: The Finite-Difference Time-Domain Method. 3. Artech House; Norwood, MA: 2005.

33. Meaney PM, Fanning MW, Li D, Poplack SP, Paulsen KD. A clinical prototype for active microwave imaging of the breast. IEEE Trans Microw Theory Tech November;2000 48(11):1841–1853.

34. Fang Q, Meaney PM, Paulsen KD. Singular value analysis of the Jacobian matrix in microwave image reconstruction. IEEE Trans Antennas Propag August;2006 54(8):2371–2380.

35. Remis RF, van den Berg PM. On the equivalence of the Newton-Kantorovich and Distorted Born methods. Inverse Problems 2000;16(1):1–4.

36. Cui TJ, Qin Y, Wang G, Chew WC. Low-frequency detection of two-dimensional buried objects using high-order extended born approximations. Inverse Problems 2004;20:S41S62.

37. Nocedal, J.; Wright, SJ. Nonlinear Optimization. 2. Springer; New York: 2006.

38. Shea, JD.; Hagness, SC.; Van Veen, BD. Hardware acceleration of FDTD computations for 3-D microwave breast tomography. Proceedings of the IEEE International Symposium on Antennas and Propagation; Charleston, SC. june 2009;

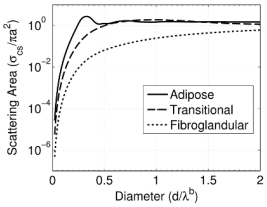

Figure 1.

Scattering cross-section of a homogeneous dielectric sphere of radius *a* as a function of diameter. The diameter of the sphere is given in units of wavelengths in the background medium, λ^b. The sphere has the properties of malignant tissue and is placed in a lossless version of three representative backgrounds: adipose, transitional, and normal fibroglandular tissues. The contrast in relative permittivity between the sphere and the background at 2.5 GHz for these three cases are 11.6, 2.55, and 1.15, respectively.

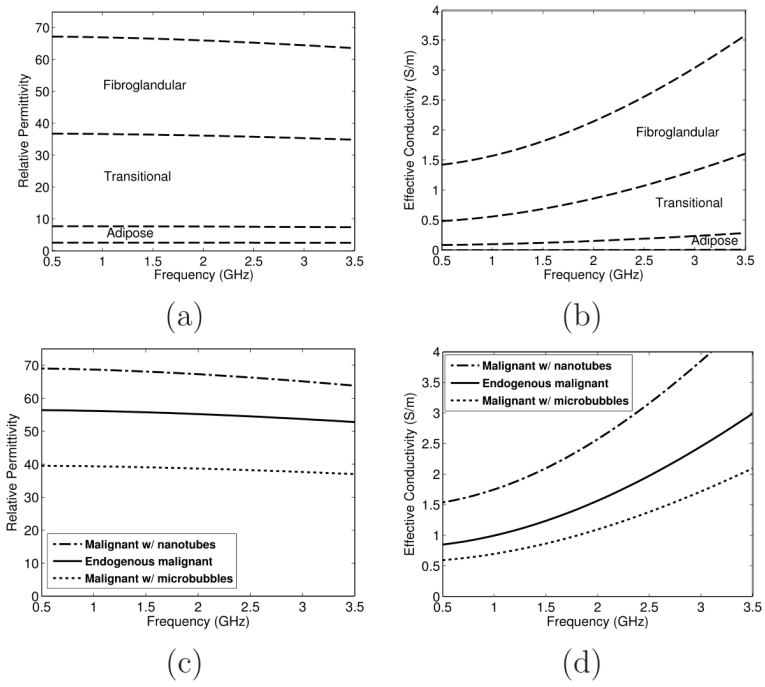

Figure 2.

(a) Relative permittivity, ε_{rel}, and (b) effective conductivity, σ_{eff} (S/m), of the ranges of adipose, transitional, and normal fibroglandular tissues used in phantom construction. (c) Relative permittivity, ε_{rel}, and (d) effective conductivity, σ_{eff} (S/m), of the malignant tissue models with and without the assumed effect of carbon nanotube or microbubble contrast agents.

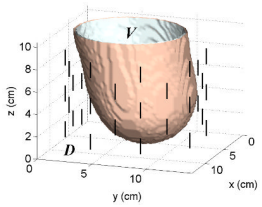

Figure 3.
Diagram of the 3-D forward solution domain for the Class 2 numerical phantom, showing the dipole array, the downsampled skin layer, the measurement region $\mathcal{D}$, and the imaging region $\mathcal{V}$ of the interior breast volume.

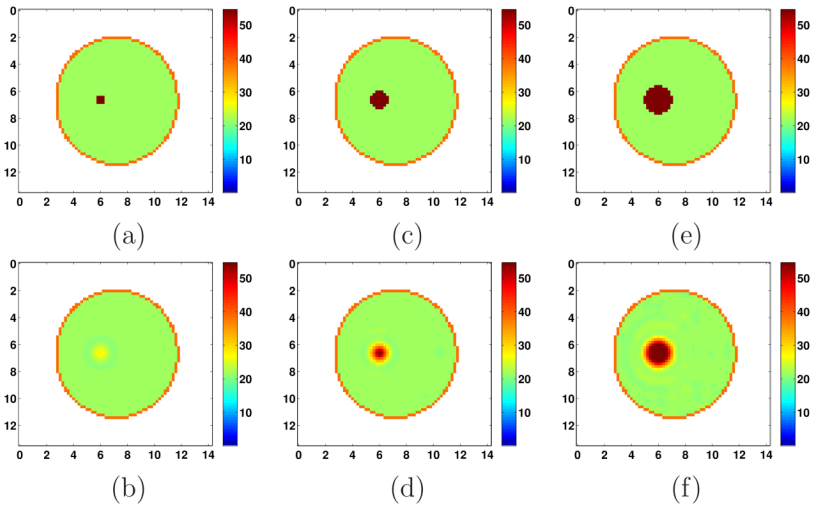

Figure 4.

Comparison of the exact (top row) and reconstructed (bottom row) coronal cross-sections (in color) of relative permittivity for a single spherical inclusion of malignant tissue properties within a homogeneous breast volume of transitional tissue properties. The inclusion diameters are (a)–(b) 6 mm, (c)–(d) 14 mm, and (e)–(f) 22 mm. Spatial smoothing of the inclusion boundary and increasing underestimation of the inclusion properties with decreasing diameter are evident in the reconstructions. (Axes in cm.)

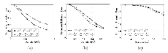

Figure 5.
The normalized error in the estimation of the dielectric properties of the spherical malignant inclusion versus diameter in a homogeneous breast interior of (a) fibroglandular tissue, (b) transitional tissue, and (c) adipose tissue. The estimate is defined as the average of the reconstructed properties over the actual inclusion volume. The error is calculated as $(u^* - u^{est})/(u^* - u^{init})$, where u is either relative permittivity, ε_{rel}, or effective conductivity, σ_{eff}, at 2.5 GHz.

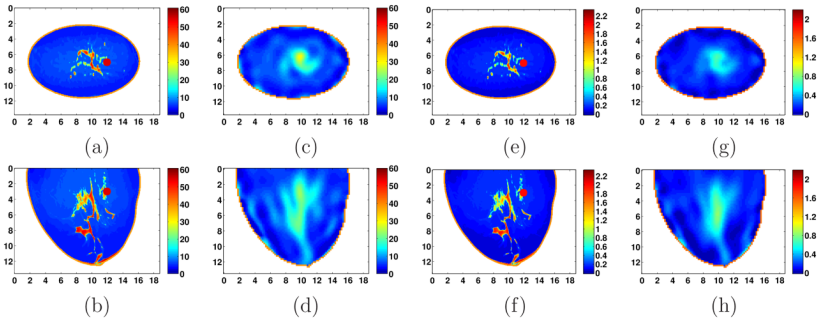

Figure 6.

Reconstruction of the Class 1 phantom with a single 1.0-cm-diameter spherical malignant inclusion. Coronal (top row) and sagittal (bottom row) cross-sections (in color) of the exact and reconstructed volumes are shown at 2.5 GHz for (a)–(d) relative permittivity and (e)–(h) effective conductivity in (S/m). (Axes in cm.)

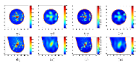

Figure 7.
Reconstruction of the Class 2 phantom with a single 1.0-cm-diameter spherical malignant inclusion. Coronal (top row) and sagittal (bottom row) cross-sections (in color) of the exact and reconstructed volumes are shown at 2.5 GHz for (a)–(d) relative permittivity and (e)–(h) effective conductivity in (S/m). (Axes in cm.)

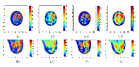

Figure 8.
Reconstruction of the Class 3 phantom with a single 1.0-cm-diameter spherical malignant inclusion. Coronal (top row) and sagittal (bottom row) cross-sections (in color) of the exact and reconstructed volumes are shown at 2.5 GHz for (a)–(d) relative permittivity and (e)–(h) effective conductivity in (S/m). (Axes in cm.)

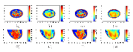

Figure 9.
Reconstruction of the Class 4 phantom with a single 1.0-cm-diameter spherical malignant inclusion. Coronal (top row) and sagittal (bottom row) cross-sections (in color) of the exact and reconstructed volumes are shown at 2.5 GHz for (a)–(d) relative permittivity and (e)–(h) effective conductivity in (S/m). (Axes in cm.)

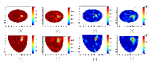

Figure 10.
Differential imaging of the Class 1 phantom using contrast agents. Coronal (top row) and sagittal (bottom row) cross-sections (in color) of the complex permittivity at 2.5 GHz are taken through the peak of the change in (a)–(b) relative permittivity and (c)–(d) effective conductivity (S/m) due to microbubble contrast agent, and the peak of the change in (e)–(f) relative permittivity and (g)–(h) effective conductivity (S/m) due to carbon nanotube contrast agent. The '×' markers show the actual location of the tumor as projected onto each cross-sectional plane. (Axes in cm.)

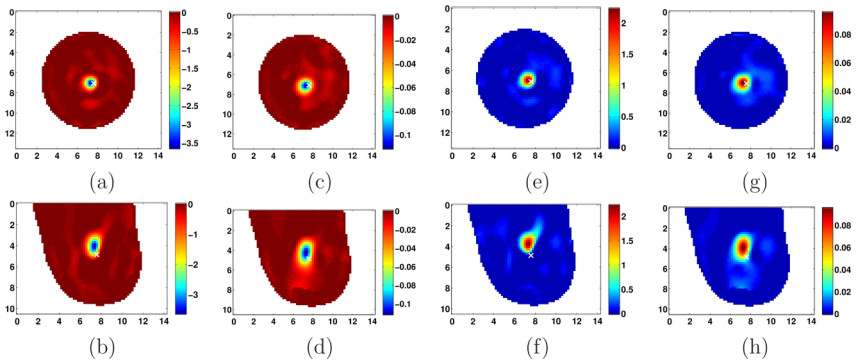

Figure 11.

Differential imaging of the Class 2 phantom using contrast agents. Coronal (top row) and sagittal (bottom row) cross-sections (in color) of the complex permittivity (S/m) at 2.5 GHz are taken through the peak of the change in (a)–(b) relative permittivity and (c)–(d) effective conductivity (S/m) due to microbubble contrast agent, and the peak of the change in (e)–(f) relative permittivity and (g)–(h) effective conductivity (S/m) due to carbon nanotube contrast agent. The '×' markers show the actual location of the tumor as projected onto each cross-sectional plane. (Axes in cm.)

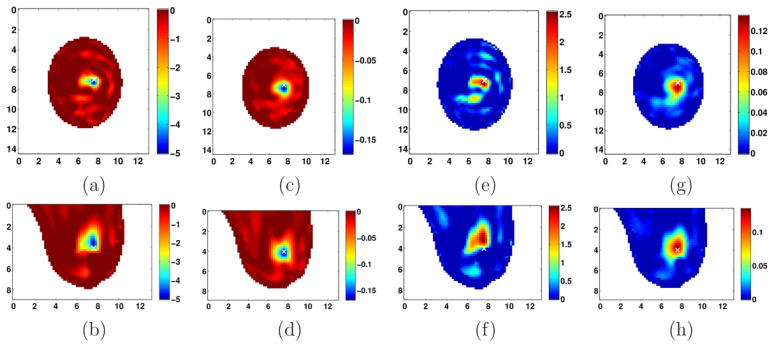

Figure 12.

Differential imaging of the Class 3 phantom using contrast agents. Coronal (top row) and sagittal (bottom row) cross-sections (in color) of the complex permittivity (S/m) at 2.5 GHz are taken through the peak of the change in (a)–(b) relative permittivity and (c)–(d) effective conductivity (S/m) due to microbubble contrast agent, and the peak of the change in (e)–(f) relative permittivity and (g)–(h) effective conductivity (S/m) due to carbon nanotube contrast agent. The '×' markers show the actual location of the tumor as projected onto each cross-sectional plane. (Axes in cm.)

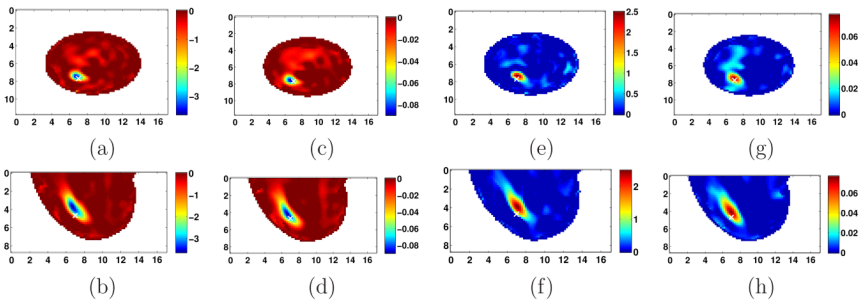

Figure 13.
Differential imaging of the Class 4 phantom using contrast agents. Coronal (top row) and sagittal (bottom row) cross-sections (in color) of the complex permittivity (S/m) at 2.5 GHz are taken through the peak of the change in (a)–(b) relative permittivity and (c)–(d) effective conductivity (S/m) due to microbubble contrast agent, and the peak of the change in (e)–(f) relative permittivity and (g)–(h) effective conductivity (S/m) due to carbon nanotube contrast agent. The '×' markers show the actual location of the tumor as projected onto each cross-sectional plane. (Axes in cm.)

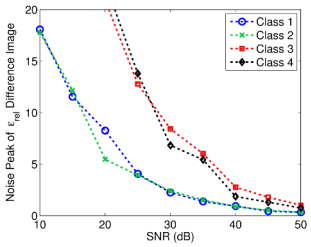

Figure 14.

Peak pertubation of relative permittivity in microbubble difference images reconstructed from noise-corrupted measurement data from each of the four heterogeneous numerical breast phantoms. The plots indicate the maximum absolute perturbation (over all voxels in $\mathcal{V}$) due to a given noise level, relative to the noiseless difference image.

Table 1

Debye parameters of the tissue models used in the construction of the numerical phantoms (valid from 0.5 to 3.5 GHz). The relaxation time constant parameter is τ=15.0 ps for all tissues.

Tissue	ε_s	ε_∞	$\Delta\varepsilon$	σ_s (S/m)
Adipose	2.42–7.63	2.28–4.09	0.141–3.54	0.0023–0.0842
Transitional	7.63–36.7	4.09–16.8	3.54–19.9	0.0842–0.461
Fibroglandular	36.7–67.2	16.8–29.1	19.9–38.1	0.461–1.38
Malignant, endogenous	56.6	18.8	37.8	0.803
with μ-bubbles	39.7	13.2	26.5	0.562
with nanotubes	69.3	14.8	54.5	1.47
Skin	40.1	15.3	24.8	0.74

Table 2

Peak contrast of estimated complex permittivity at 2.5 GHz of a malignant spherical inclusion in a homogeneous breast interior. For reference, the electrical size of the inclusion diameter in each background tissue is given in wavelengths.

		Peak Estimated Contrast (inclusion diameter)					
Background	**Exact Contrast**	**(2 mm)**	**(6 mm)**	**(10 mm)**	**(14 mm)**	**(18 mm)**	**(22 mm)**
Fibroglandular,		(0.11λ)	(0.34λ)	(0.57λ)	(0.80λ)	(1.03λ)	(1.26λ)
$\max(\varepsilon_{\text{rel}}/\varepsilon_{\text{rel}}^{b})$	1.15	1.00	1.05	1.10	1.17	1.18	1.19
$\max(\sigma_{\text{eff}}/\sigma_{\text{eff}}^{b})$	1.13	1.00	1.03	1.07	1.12	1.14	1.15
Transitional,		(0.08λ)	(0.23λ)	(0.39λ)	(0.54λ)	(0.70λ)	(0.85λ)
$\max(\varepsilon_{\text{rel}}/\varepsilon_{\text{rel}}^{b})$	2.55	1.02	1.27	1.77	2.57	2.98	2.88
$\max(\sigma_{\text{eff}}/\sigma_{\text{eff}}^{b})$	2.99	1.02	1.28	1.78	2.47	2.73	2.94
Adipose,		(0.04λ)	(0.11λ)	(0.18λ)	(0.25λ)	(0.33λ)	(0.40λ)
$\max(\varepsilon_{\text{rel}}/\varepsilon_{\text{rel}}^{b})$	11.6	1.01	1.12	1.39	2.16	5.25	9.16
$\max(\sigma_{\text{eff}}/\sigma_{\text{eff}}^{b})$	22.1	1.01	1.17	1.57	2.71	7.15	16.3

Table 3

Changes in dielectric properties and location errors at 2.5 GHz in the differential imaging of a 1.0-cm-diameter malignant spherical inclusion in realistic heterogeneous phantoms using microbubble and carbon nanotube contrast agents.

Phantom		Exact Change (%)		Est. Change (%)		$\|\|\hat{\mathbf{r}} - \mathbf{r}^*\|\|$ (mm)	
Class	**Agent**	ε_{rel}	σ_{eff}	ε_{rel}	σ_{eff}	ε_{rel}	σ_{eff}
1	μ-bubble	−30	−30	−1.8	−1.2	4.5	2.8
	nanotube	+22	+60	+0.9	+0.8	6.0	3.5
2	μ-bubble	−30	−30	−6.6	−5.6	8.2	7.2
	nanotube	+22	+60	+4.1	+4.8	12	11
3	μ-bubble	−30	−30	−9.1	−8.5	4.5	4.5
	nanotube	+22	+60	+4.6	+6.8	8.2	4.5
4	μ-bubble	−30	−30	−6.6	−4.5	8.5	7.5
	nanotube	+22	+60	+4.6	+3.9	8.9	6.3

Algorithm 1

Gauss-Newton for Distorted Born Iterative Method

$i \leftarrow 0$

$\widetilde{\boldsymbol{\varepsilon}}_0^b \leftarrow$ initial background profile

repeat

for $m = 1$ to N **do**

FDTD: $\mathbf{E}^b(\mathbf{r}_n|\mathbf{r}_m)$ for $n = 1, \ldots, N$; $\mathbf{E}^b(\mathbf{r}_k|\mathbf{r}_m)$ and $\bar{\mathbf{G}}^b(\mathbf{r}_k|\mathbf{r}_m)$ for $k = 1, \ldots, K$

$\mathbf{E}^s(\mathbf{r}_n|\mathbf{r}_m) \leftarrow \mathbf{E}^{meas}(\mathbf{r}_n|\mathbf{r}_m) - \mathbf{E}^b(\mathbf{r}_n|\mathbf{r}_m)$ for $n = 1, \ldots, N$

$\bar{\mathbf{G}}^b(\mathbf{r}_m|\mathbf{r}_k) \leftarrow \bar{\mathbf{G}}^b(\mathbf{r}_k|\mathbf{r}_m)^T$ for $k = 1, \ldots, K$

end for

construct $\mathbf{A}_i$, $\mathbf{y}_i$

$\hat{\mathbf{x}}_i \leftarrow \mathrm{CGLS}(\mathbf{A}_i, \mathbf{y}_i)$

$\widetilde{\boldsymbol{\varepsilon}}_{i+1}^b \leftarrow \widetilde{\boldsymbol{\varepsilon}}_i^b + \mathcal{F}(\hat{\mathbf{x}}_i)$

$i \leftarrow i + 1$

until $\|\mathbf{y}_{i-1}\| - \|\mathbf{y}_i\| < \delta \|\mathbf{y}_0\|$